Quantum wave packet dynamics with trajectories: Implementation with adaptive Lagrangian grids

Robert E. Wyatt
Institute for Theoretical Chemistry, Department of Chemistry and Biochemistry, The University of Texas, Austin, Texas 78712

Eric R. Bittner
Department of Chemistry, The University of Houston, Houston, Texas 77204

(Received 14 July 2000; accepted 1 September 2000)

The quantum trajectory method was recently developed to solve the hydrodynamic equations of motion in the Lagrangian, moving-with-the-fluid, picture. In this approach, trajectories are integrated for fluid elements (''particles'') moving under the influence of the combined force from the potential surface and the quantum potential. To accurately compute the quantum potential and the quantum force, it is necessary to obtain the derivatives of a function given only the values on the unstructured mesh defined by the particle locations. However, in some regions of space–time, the particle mesh shows compression and inflation associated with regions of large and small density, respectively. Inflation is especially severe near nodes in the wave function. In order to circumvent problems associated with highly nonuniform grids defined by the particle locations, adaptation of moving grids is introduced in this study. By changing the representation of the wave function in these local regions (which can be identified by diagnostic tools), propagation is possible to much longer times. These grid adaptation techniques are applied to the reflected portion of a wave packet scattering from an Eckart potential. © *2000 American Institute of Physics.*
[S0021-9606(00)01244-7]

I. INTRODUCTION

The hydrodynamic formulation of quantum mechanics[1–8] leads to a description of the time-evolution of the probability density, wave function, and other quantities in terms of equations-of-motion which have analogies to those developed for classical compressible fluids. Studies in quantum hydrodynamics fall into two domains having different methodologies and goals. The older and possibly better known approach uses quantum hydrodynamics as an analytical tool. Typically, this approach is initiated by first solving the time-dependent Schrödinger equation to obtain the wave function. In the second step, analysis is performed on this wave function to yield hydrodynamic quantities such as flux maps and particle trajectories.[7] An example of this approach is analysis of the double-slit diffraction problem in terms of Bohm trajectories and the way in which they are influenced by the quantum potential.[7,9] The second and less developed strategy is quite different. In contrast to the analytical route mentioned previously, the synthetic approach is based upon the direct solution of the hydrodynamic equations-of-motion so as to propagate discretized elements of the probability fluid.[10–18] During the propagation, the wave function may be computed ''on-the-fly,'' but it is not presupposed as in the analytical approach.

The quantum trajectory method (QTM), introduced recently by Lopreore and Wyatt, is an example of the synthetic approach.[12] An approach similar to the QTM has also been recently developed by Sales Mayor *et al.*[13] In the QTM, the equations-of-motion for discretized fluid elements (''particles'') are formulated and solved in the Lagrangian, moving-with-the-fluid, picture. These fluid elements follow quantum trajectories which are influenced by both the classical force obtained from the potential energy surface and the quantum force obtained from the Bohm quantum potential, Q. The quantum potential measures the curvature of the amplitude of the wave function around each of the particles and in this formulation is the source of all quantum effects. The main approximation involves the use of a relatively small number of fluid elements, although additional approximations may be introduced in the computational implementation.

The QTM has been applied to barrier transmission,[12] nonclassical reflection from a downhill ramp,[14] and a collinear model chemical reaction.[15] It has also been shown how the wave function, including phase information, may be generated along the quantum trajectories.[16] Also, distributed approximating functionals,[17,18] DAFs, have been implemented in the QTM in order to provide an accurate evaluation of Q and its derivatives.[19] In addition, Bittner has developed and applied related methods to study tunneling dynamics in the double well potential.[20] In related earlier studies, Weiner *et al.*[10,11] used a Lagrangian hydrodynamic approach to study the motion of Gaussian wave packets on quadratic potential surfaces.

In a companion to the present study, Bittner and Wyatt presented three enhancements to the quantum hydrodynamic methodology.[21] These included a technique for propagating quantum trajectories perpendicular to wavefronts (surfaces of constant quantum action, S), a method for propagating least squares expansion coefficients, and the use of local gauge

transformations to remove fast components of the wave function, so that the accuracy of computed derivatives would be improved. In the present study, the focus will be upon the introduction and implementation of local adaptive Lagrangian grids. These local grids are carried along with the particles exterior to the local grid and they are introduced in some internal regions over certain time intervals in order to avoid the difficulty of computing the quantum potential and the quantum force near wave function nodes. In fact, moving local meshes can eliminate difficulties encountered around wave function nodes, at the expense of stepping outside the traditional formulation of quantum hydrodynamics. In addition, adaptive grids can be used to redistribute mesh points to improve the sampling of data (such as the probability density or the velocity) that is being carried along by the moving particles. (The terms ''mesh points'' and ''particles'' will be used interchangeably in this study.)

Mesh adaptation continues to be a topic of intense investigation in computational fluid dynamics[22–28] and some of the techniques used in this study have their origin in classical fluid dynamics. A subsidiary aspect of mesh adaptation concerns the issues of where and when the adapted mesh should be used. For this purpose, diagnostic tools are needed to signal the early onset of regions where problems may occur at later times. The diagnostic problem will also be addressed in this study.

The way in which the adapted mesh is used is as follows. Assume that N quantum trajectories have been generated up to time T in a scattering calculation. At this time, a diagnostic indicator has sensed impending trouble within a region denoted Γ. The adapted mesh is introduced within Γ and whatever information carried by the particles (probability density, wave function phase, velocity,...) is interpolated onto the new mesh. The number of new mesh points within Γ may be different from the number of particles that were there originally. As a result, when we propagate forward in time, we are no longer following the trajectories of the original particles, although these could be obtained by interpolation. In any case, for particles not within Γ, the usual hydrodynamic equations-of-motion are solved to update the particle positions and other quantities. However, for those particles within Γ, in order to maintain accuracy in the propagation, it may be essential not to use the hydrodynamic representation. By some means (to be described later in Sec. V B), the wave function is updated to obtain the value at each new mesh point within Γ. This completes the first time step after mesh adaptation so that the cycle may then be repeated. The exterior particles move along from time step to time step, and mesh adaptation-interpolation-propagation is performed within the moving region Γ. This whole process in repeated until the diagnostic indicators have calmed down enough to continue with the global hydrodynamic propagation.

The outline of the present study is as follows. In Sec. II, the formulation of Lagrangian quantum hydrodynamics will be reviewed and the role played by the quantum trajectories will be described. At the end of this section, a description is presented of the model one-dimensional scattering problem that will be used as an example for grid adaptation. In Sec. III, the origins of irregular spacings between the particles are considered, with special emphasis upon particle dynamics near wave function nodes. Section IV describes adaptation strategies for Lagrangian grids, including the design and use of diagnostic tools. In Sec. V, alternative representations of the wave function are defined; it will be necessary to change representations in certain regions in order to avoid computational problems encountered when using the hydrodynamic representation near nodes in the wave function. In Sec. VI, computational results obtained using grid adaptation will be presented for the reflected portion of a wave packet which has scattered from a repulsive Eckart potential. The transmitted portion of the wave packet experiences no computational problems when the QTM is used to propagate quantum trajectories; this aspect of the dynamics is the subject of a previous study.[19] However, in the reflected region, a number of nodes develop at later times and it is in this region that the grid adaptation strategies will be implemented. Finally, concluding remarks are presented in Sec. VII.

II. LAGRANGIAN QUANTUM HYDRODYNAMICS

In this section, a brief review of the quantum trajectory method[12,14–16,19] will be presented (also see Ref. 13). We begin by expressing the time-dependent wave function in exponential form, $\Psi(\mathbf{r},t)=e^{i\xi/\hbar}$. The complex-valued phase is $\xi(\mathbf{r},t)=-i\hbar C(\mathbf{r},t)+S(\mathbf{r},t)$, where both C (the C-amplitude) and S (the action function) are real-valued. The wavefunction may also be written in polar form, $\psi(\mathbf{r},t)=R(\mathbf{r},t)e^{iS(\mathbf{r},t)/\hbar}$, so that the probability density is then given by either of two expressions, $\rho(\mathbf{r},t)=e^{2C(\mathbf{r},t)}=R(\mathbf{r},t)^2$. The advantage of using the exponential form is that C and S are frequently slowly varying, even when the real and imaginary parts of Ψ are rapidly oscillating. However, near some points, the preceding statement is not correct and as a result the advantage in using R or C and S is lost; elaboration of this statement is provided in the next section. After substituting the exponential expression for Ψ into the time-dependent Schrödinger equation, we obtain the equations-of-motion for the two scalar fields

$$\frac{\partial C}{\partial t}=-\frac{1}{2}\nabla\cdot\mathbf{v}-\mathbf{v}\cdot\nabla C, \tag{1}$$

$$-\frac{\partial S}{\partial t}=\frac{1}{2m}|\nabla S|^2+V+Q, \tag{2}$$

where the current velocity is $\mathbf{v}(\mathbf{r},t)=(1/m)\nabla S(\mathbf{r},t)$. The second of these equations is the quantum Hamilton–Jacobi equation (QHJ), which differs from the classical HJ equation by the presence of the Bohm quantum potential,

$$Q(\mathbf{r},t)=-\frac{\hbar^2}{2m}\{\nabla^2 C+|\nabla C|^2\}. \tag{3}$$

Rather than attempt to solve the QHJ equation, we take the gradient of Eq. (2) and obtain a Newtonian-type equation for the flow acceleration,

$$m\left\{\frac{\partial}{\partial t}+\mathbf{v}\cdot\nabla\right\}\mathbf{v}=-\nabla(V+Q), \tag{4}$$

where the two terms on the right-hand side are the ''classical'' force obtained from the gradient of the potential and the quantum force obtained from the gradient of the quantum potential. Equations (1) and (4) are then used to update the flow velocity and the C-amplitude, which in turn is needed to update the quantum potential in Eq. (3).

Equations (1) and (4) for C and $\mathbf{v}$ are expressed in the Eulerian picture; the fields evolve with respect to a fixed-in-space coordinate system. We now convert to the Lagrangian picture by introducing a local frame moving with the fields. This is done by utilizing the time derivative expressed in the moving frame, $d/dt=\partial/\partial t+\mathbf{v}\cdot\boldsymbol{\nabla}$, where the second term is the convective contribution. Equations (1) and (4) in the Lagrangian picture are then

$$\frac{dC}{dt}=-\frac{1}{2}\boldsymbol{\nabla}\cdot\mathbf{v}, \tag{5}$$

$$\frac{d\mathbf{v}}{dt}=-\frac{1}{m}\boldsymbol{\nabla}V+\frac{\hbar^2}{2m^2}\boldsymbol{\nabla}\{\nabla^2 C+|\boldsymbol{\nabla}C|^2\}. \tag{6}$$

In these equations, the convective operator $\mathbf{v}\cdot\boldsymbol{\nabla}$ no longer appears explicitly.

The Lagrangian hydrodynamic equations are solved by discretizing the probability fluid in terms of N fluid elements, termed ''particles.'' Equations (5) and (6) and then integrated to find quantum trajectories for the fluid elements. The position of each particle is obtained by integrating $d\mathbf{r}=\mathbf{v}dt$ along with Eqs. (5) and (6). It is important to note that the trajectory for each fluid element is correlated with the trajectory for each of the other fluid elements. However, when the quantum force becomes very small or vanishes, the fluid elements move as a classical uncorrelated ensemble. When Eq. (5) is integrated along the trajectory, we obtain for the C-amplitude,

$$C(\mathbf{r},t)=C_0(\mathbf{r}_0)-\frac{1}{2}\int_0^t\boldsymbol{\nabla}\cdot\mathbf{v}dt, \tag{7}$$

where $C_0(\mathbf{r})$ and $\mathbf{r}_0$ are the initial values at $t=0$. The divergence of the velocity field in the integrand is a function of time and is evaluated along the trajectory $\mathbf{r}(t)$.

The action function does not appear explicitly in Eqs. (5) and (6), but its gradient does, through the proportionality between $\mathbf{v}$ and $\boldsymbol{\nabla}S$. As each trajectory is integrated, the action function can be obtained by integrating the quantum Lagrangian along the trajectory.[16] The quantum Lagrangian, L_q, is the excess of the flow kinetic energy over the total potential, $L_q(t)=(1/2)mv^2-(V+Q)$. The time-dependent action along the trajectory is then given by

$$S(t)=S_0+\int_0^t L_q(\tau)d\tau. \tag{8}$$

Equations (6)–(8) are the working equations used to update the position, velocity, C-amplitude, and action.

In this study, grid adaptation will be applied to the time-dependent one-dimensional scattering of an initial Gaussian wave packet from a repulsive Eckart potential. The Eckart potential is given by $V(x)=V_0\,\mathrm{sech}^2[a(x-x_b)]$, where $V_0=8000\,\mathrm{cm}^{-1}$ is the barrier height, $a=0.4$ determines the width, and $x_b=7.0$ a.u. is the location of the barrier maximum. The mass used in these calculations is $m=2000$ a.u. and the time step is $\Delta t=4$ a.u. For the results reported in Sec. VII, 120 fluid elements were used (with the initial nearest neighbor spacing 0.04 a.u.). As time proceeds, the wave packet moves toward the barrier and eventually splits into reflected and transmitted wave packets. Emphasis will be placed upon grid adaptation for the reflected wave packet, which is where nodes form.

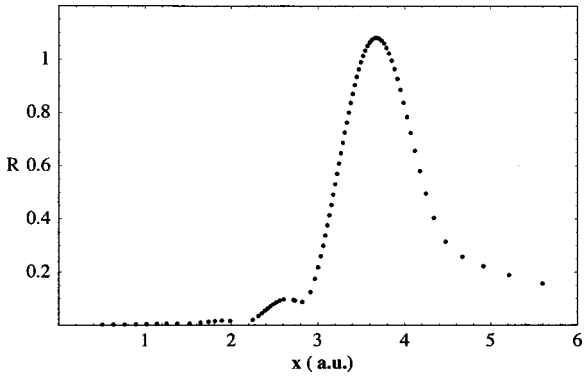

FIG. 1. Amplitude function $R(x)$ for wave packet scattering from an Eckart barrier at time step 470 ($t=45.5$ fs). The dots show the function values at the particle positions. The Eckart barrier is centered to the right of the figure at 7.0 a.u.

At time $t=0$, the initial wave packet is the product of a Gaussian shape factor and a plane wave driving term

$$\Psi(x,0)=(2\beta/\pi)^{1/4}e^{-\beta(x-x_0)^2}e^{ik(x-x_0)}, \tag{9}$$

where β is the width factor for the Gaussian, and where k determines the initial phase and flow kinetic energy, $S_0=\hbar k(x-x_0)$ and $E=\hbar^2k^2/(2m)$. This wave packet has the width parameter $\beta=4.0$ a.u., is centered at $x_0=2.0$ a.u., and has the initial translational energy of 4000 cm^{-1}. From Eq. (9), the initial condition on the C-amplitude is $C_0(x)=\ln(2\beta/\pi)^{1/4}-\beta(x-x_0)^2$. Finally, the fluid elements are initiated with the same speed, $v=(1/m)\partial S_0/\partial x=\hbar k/m$.

III. DENSITY FLUCTUATIONS AND PARTICLE DYNAMICS NEAR NODES

A. Compression and inflation

At each time step, the particle positions $\{x_i(t)\}$ define a moving and unstructured grid. Typically, we start at $t=0$ with all of the nearest neighbor spacings having the same value. However, after several time steps, the spacings are no longer uniform. As time proceeds, this nonuniformity includes local features categorized as compression or inflation.

Examples of regions where there is compression and inflation are shown in Fig. 1. Each dot in this figure shows the value of the amplitude $R(x)$ at the position of each of 79 particles at time step 470 (where each time step $\Delta t=4$ a.u. $=0.097$ fs) for the one-dimensional scattering of an initial Gaussian wave packet from an Eckart barrier centered at $x_b=7.0$ a.u. At this time step the main part of the packet is reflecting back to the left of the figure in the direction from which the initial wave packet was launched toward the barrier. The portion of the wave packet (involving the remaining

41 particles) for $x>7.0$ a.u. is not shown in this figure. Compression refers to the high density of particles which develop at local maxima in the amplitude; this occurs near $x=2.6$ a.u. and $x=3.6$ a.u.

The term inflation was used recently by Pinto-Neto and Santini[29] in reference to the influence of the quantum force on Bohm trajectories near the singularity at $t=0$ in the Wheeler–DeWitt equation, which was analyzed as a model quantum cosmology. Analogous behavior occurs in the wave packet scattering problem; as nodes or quasinodes develop, nearby trajectories move away from the region where $R(x)$ is heading toward zero. [The term quasinode refers to a region where $R(x)$ reaches a local minimum and attains a small value but does not become exactly zero. Quasinodes include prenodes and postnodes; during the course of time, a prenode evolves into a postnode. Frequently, the sequence prenode→node→postnode occurs, but in some cases the exact node may not form, so that the sequence is prenode→postnode.] The increased separation of initially nearby particles as they move away from the node is a manifestation of inflation. The source of this expansion is the quantum potential, which becomes singular at an exact node. [This is true unless $\nabla^2 R$ also happens to vanish, in which case the singularity is canceled. This follows because, in terms of the R-amplitude, $Q=(-\hbar^2/(2m))R^{-1}\nabla^2 R$.] As a result of inflation, the particles are unlikely to be found close to the nodes or quasinodes. An example is shown in Fig. 1; the particle density near the quasinode at $x=2.1$ a.u. is very low. Similar behavior is observed at the two quasinodes located near $x=1.5$ and 2.8 a.u.

The net result of compression and inflation is that the interparticle spacings become very nonuniform. This leads to a sampling problem: there is an oversupply of information in some regions while not enough is available in other regions. Adapting the mesh defined by the particle locations to the local (in both space and time) conditions (density fluctuations) can alleviate this problem.

B. Trajectory dynamics near nodes

In order to appreciate the difficulties that wave function nodes cause when attempting to integrate quantum trajectories, several features of the dynamics near one node will be examined. This node develops in the dynamics near $x=3.1$ a.u. close to time step 457. This node preceeds the main part of the reflected wave packet that has undergone scattering with the Eckart barrier. Starting about time step 420, a prenode begins to form and as time proceeds, this prenode gradually evolves into the node that was referred to at time step 457. After this time, the node reverts to a postnode and then gradually disappears by about time step 520. The whole process of nodal formation and decay thus takes place within about 100 time steps. [The node near $x=3.1$ a.u. in Fig. 2(b) gradually heals as it moves to the left and later appears in Fig. 1 as the postnode near $x=2.8$ a.u.]

It is well known that quantum trajectories cannot cross nodal surfaces.[7] However, this statement does not apply to quasinodes. As a prenode gradually forms before the node develops, particles can cross from one side to the other, and this also happens as the postnode decays. Since the true (''exact'') node is formed at only one instant of time, the fact that particles cannot cross nodal surfaces is of little consequence. However, what *is* significant is that inflation occurs during the whole process of quasinode–node formation and decay. Particles are forced away from the ''center'' of the quasinode because the quantum force imparts to them a high velocity, so that when they cross the center they must do so very quickly.

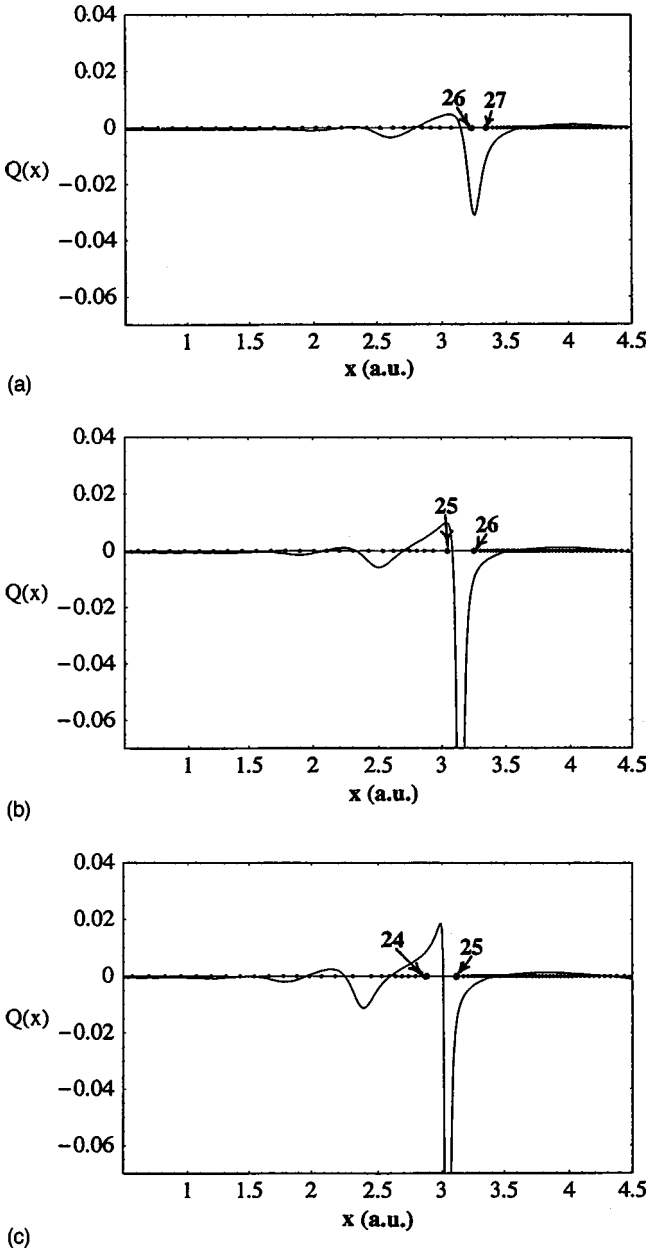

FIG. 2. Quantum potential (continuous curve) and locations of particles (dots on horizontal axis) for time steps (a) 440, (b) 450, and (c) 460. The indices for the two particles located on either side of the center of the quasinode are indicated.

These features are illustrated in Fig. 2, which shows the quantum potential and the locations of the reflected particles in the region surrounding the node that develops at $x=3.1$ a.u. close to time step 457. Three time steps are shown, steps 440, 450, and 460 in parts (a), (b), and (c), respectively.

On time step 440, particles 1–26 are to the left of the center of the prenode, and particles 27–120 are to the right. Inflation near the center of the prenode at $x=3.2$ a.u. and compression to the right of that position are evident. Just before this time step particle 27 crossed from the left to the right of the center. Advancing to time step 450 in part (b), particle 26 has just joined the particles to the right of the center, and particle 25, now located just to the left of the center is about to join those on the right. On time step 460 shown in part (c), just after the node starts to decay, particles 25–120 are located on the right of the center of the postnode. After this time step, inflation near the center diminishes, as the postnode gradually heals. It is clear from the analysis of the birth–death history of the node near $x=3.1$ a.u. that during inflation, a few particles can hop from one side of the quasinode to the other.

Transport of a few particles from one side of the quasinode to the other presents problems because of the interconnected issues of inflation and sampling. When particles inflate away from the center of the quasinode, accurate computation of the quantum potential and the quantum force, $f_q=-\nabla Q$, is extremely difficult. In this region, both Q and f_q vary rapidly and because particles on opposite sides of the quasinode are relatively far apart, most numerical methods for computing accurate derivatives are doomed. It is for this reason that adaptive grid techniques will be introduced in the next section.

Analysis of the quantum potential for small displacements from the center of the quasinode is relatively straightforward. For example, for time step 457 (close to the time when the ''exact'' node forms), the amplitude $R(x)$ is shown in Fig. 3(a). Near the center of the node at position x_0, consider the Taylor expansions in regions I and II to the left or the right of the quasinode, respectively ($y=x-x_0$),

$$\begin{aligned} R_1(y)&=a+by+cy^2+dy^3 \quad \text{region I} \quad (x<x_0),\\ R_2(y)&=a+ey+fy^2+gy^3 \quad \text{region II} \quad (x>x_0). \end{aligned} \tag{10}$$

In order to match the shape of $R(x)$ and the first two derivatives in the two separate regions, we will assume that $b<0$, $c<0$, $d<0$ and $e>0$, $f>0$, and $g<0$. From these equations, the quantum potential in regions I and II is given by ($A=-\hbar^2/(2m)$),

$$\begin{aligned} Q_1(y)&=A(2c+6dy)/(a+by+cy^2+dy^3) \quad \text{region I},\\ Q_2(y)&=A(2f+6gy)/(a+ey+fy^2+gy^3) \quad \text{region II}. \end{aligned} \tag{11}$$

At the minimum of the quasinode ($y=0$), $Q_1(0)=2Ac>0$, and $Q_2(0)=2Af<0$. The quantum potential from this model is discontinuous at x_0 and this feature is shared with the numerically computed $Q(x)$ shown in Fig. 3(b). This type of analysis is useful in relating the shape of $R(x)$ near a node to the features of $Q(x)$.

IV. MOVING GRIDS AND ADAPTATION STRATEGIES

A. Adaptation of Lagrangian grids

Grid adaptation in computational fluid dynamics is an area of intense interest that is rich with ideas that can be adapted into quantum hydrodynamics.[22–27] Adaptation of Lagrangian grids defined by the instantaneous particle positions requires consideration of several overlapping issues. The purpose is to change the local separations of the particles that define the moving mesh in order to provide a better balance between regions with fine scale features and other regions with coarse features where a high particle density is not needed. We will let ΔN denote the change in the number of grid points in region Γ as a result of grid adaptation. For Lagrangian grids, this adaptation region moves with the flow; the situation here is different from Eulerian adaptation where grid points in a fixed-in-space region undergo adaptation. There are now three cases to consider.

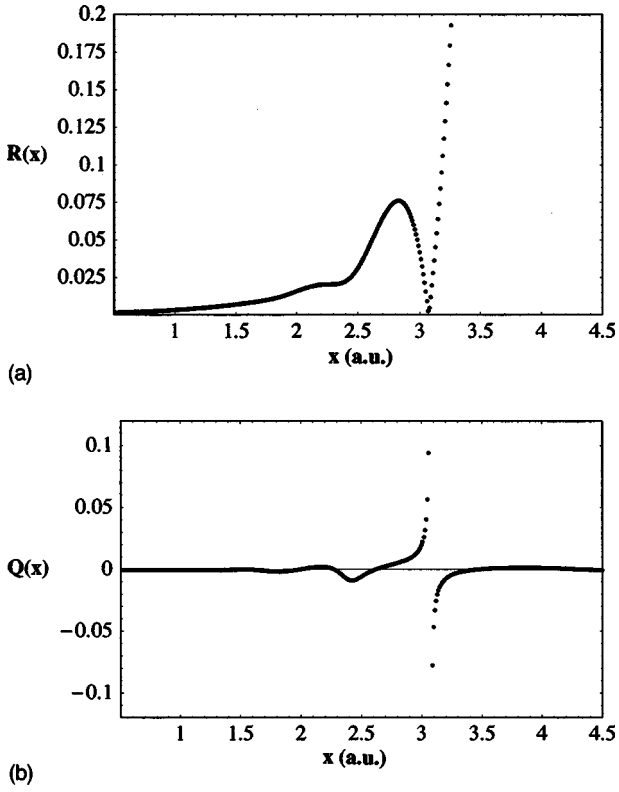

FIG. 3. Wave function amplitude (a) and quantum potential (b) for time step 457.

(a) Redistribution ($\Delta N=0$) is a useful technique for moving mesh points to more desirable locations while keeping the total number of mesh points constant. Redistribution is relatively simple to implement and does not require complicated updating of the data structures that store information carried along with each particle. An example of redistribution is shown in Fig. 4. The top row shows the positions of the particles for the discretized wave packet illustrated earlier in Fig. 1. Regions of low density due to quasinode formation between $x=2$ a.u. and $x=3.2$ a.u. are evident as are several compressive regions of high particle density. The second row in this figure shows the particle locations after redistribution. In this example, the particles with indices $M_0, M_0+1, \ldots, M_1$ were redistributed so as to make the nearest neighbor spacings equal. This redistribution was then repeated at each of 40 time steps leading to the last row in Fig. 4.

(b) Creation ($\Delta N>0$) adds particles to region Γ in order

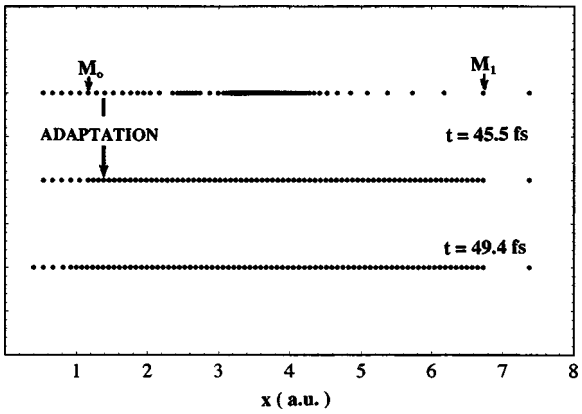

FIG. 4. Illustration of mesh redistribution. In the top row, the initial particle positions are shown before adaptation for the wave packet at time step 470. In the middle row, the points between $M_0=6$ and $M_1=81$ have been redistributed so that the nearest neighbor spacings are equal. In the bottom row, the adapted grid is shown 40 time steps later. All of the particles with $x<7.0$ a.u. are moving to the left, away from the center of the Eckart barrier.

to resolve local features of the flow field. An example of this type of adapted region is shown in Fig. 5. Ten particles with equal nearest neighbor spacings were added between the particles with indices M_0 and M_1. The particle spacings exterior to this region are not equal. The other notation on this figure will be explained later in Sec. V A.

(c) Annihilation or coarsening ($\Delta N<0$) removes particles in order to compensate for compression. Annihilation may also be used to remove particles that were created at an earlier time, assuming that they are no longer needed in the region Γ.

There are several additional points that should be kept in mind. (1) When mesh points are moved, created, or annihilated, the current data must be interpolated onto the new mesh points. (2) Both creation and annihilation require nontrivial updating of the data structures and the dimensions of some of the storage arrays will change. This adds to the computational overhead and for this reason it might be advisable to avoid doing this at every time step during the integration process. (3) For all three adaptation cases, particle trajectories are no longer followed within region Γ (but they could be through interpolation). (4) As the particles exterior to region Γ evolve to new locations, the mesh points within this region follow along, but the particles may be periodically redistributed in order to avoid inflation or compression that might otherwise occur.

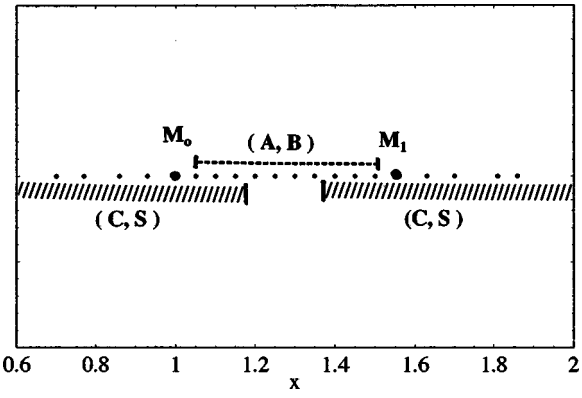

FIG. 5. Illustration of mesh adaptation. Between points M_0 and M_1, 10 equally spaced mesh points have been created. The hydrodynamic (C,S) representation is used for the exterior points 1–8 and 13–20, while the (A,B) wave function representation is used for the internal points 6–15. In the two overlap patches containing points 6–8 and 13–15, the average of the wave functions computed separately in the two regions may be used.

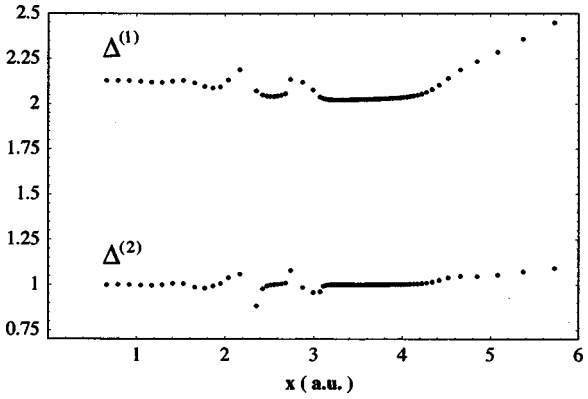

FIG. 6. Illustration of the finite difference test functions for the wave packet shown earlier in Fig. 1. For clarity, $\Delta^{(1)}$ has been shifted up by 2.0 units and $\Delta^{(2)}$ has been shifted up by 1.0 unit.

B. Diagnostic tools

Over some time intervals, local adapted grids can be used in one or more of the regions spanned by the particles. How can these regions be identified for special consideration, before the situation gets too serious? For this purpose, heuristic tools will be used to signal the onset of node formation so that adapted grids can be introduced before encountering numerical problems connected with the calculation of derivatives. There are a number of ways in which this may be done. We seek local test functions that are simple to implement such that when the value of the test function exceeds a threshold value, grid adaptation can begin automatically. In addition, at later times, it may be that fine-scale features are no longer present, so that fewer grid points would suffice. The test functions should also be able to identify this case.

For one-dimensional problems, two functions that meet these requirements are the forward first-order finite difference and central second-order finite difference (multidimensional extensions are easily defined)

$$\Delta_i^{(1)}=x_{i+1}-x_i\,,$$
$$\Delta_i^{(2)}=\Delta_i^{(1)}-\Delta_{i-1}^{(1)}=x_{i+1}+x_{i-1}-2x_i\,. \tag{12}$$

These finite differences are closely related to approximations to the first and second derivatives of the particle coordinates with respect to the particle label (i). Note that these relations are used for qualitative purposes only and do not constitute approximations that are used for computing derivatives.

These two finite difference functions are plotted vs x_i in Fig. 6 for the same discretized wave packet that was shown earlier in Fig. 1. Note that $\Delta^{(1)}$ and $|\Delta^{(2)}|$ both reach local maxima at the positions of the quasinodes in Fig. 1. As a result, the region between $x=2.0$ a.u. and $x=3.2$ a.u., where

two quasinodes have developed, should be considered for grid adaptation. However, for the ''weak'' quasinode near $x=1.5$ a.u., the two diagnostic functions do reach local maxima, but the decision on whether to adapt the local grid near this point is ambiguous.

To automatically signal the adaptation routine, a threshold criterion can be introduced. For example, we could require that the local test function exceed a certain predetermined value, such as $|\Delta_i^{(2)}|>\xi$. The value for ξ would have to be determined through experience gained on related problems. The size of the region subjected to mesh adaptation can be based upon a function of the full-width of the local maxima in the test functions.

V. ALTERNATIVE REPRESENTATIONS FOR THE WAVE FUNCTION

A. (*R,S*) and (*A,B*) representations

In Sec. II, the polar representation of the wave function was used to develop the equations-of-motion for the hydrodynamic formulation. In this Madelung representation of the wave function, the amplitude R and the gradient of the action function ∇S play a dominant role. We will refer to this as the (R,S) representation. A slightly different way to represent the wave function is through the exponentiated R-amplitude, $R=\exp(C)$. In many regions, the C-amplitude has a low degree polynomial dependence upon the coordinates and is preferred because of the ease with which accurate derivatives may be computed. For the tails of wave packets, this representation is especially useful. The hydrodynamic equations-of-motion may be derived in either of these representations, although the expressions for the quantum potential are different in the two cases.

In spite of the usefulness of the hydrodynamic (C,S) and (R,S) representations, there is one important situation where they are not very useful. This occurs near nodes, where the first derivative of R is discontinuous and where C is singular. An example is shown if Figs. 7(a) and 7(b) for the reflected portion of same wave packet that was shown earlier in Fig. 1, but at a later time step (510). Parts (a) and (b) of this figure show $R(x)$ and $C(x)$ near the quasinode that has formed near $x=1.12$ a.u. Computation of the second derivatives of $R(x)$ or $C(x)$, which are needed in order to compute the quantum potential, are likely to be inaccurate unless special precautions are taken.

In order to circumvent the computation of derivatives of R or C near nodes, we will utilize a third representation of the wave function. If we break the complex-valued wave function into real and imaginary parts, $\psi=A+iB$, then A and B and their derivatives are always well-behaved (continuous and nonsingular), even near quasinodes and nodes. This will be referred to as the (A,B) representation. For the same scattering conditions used for Figs. 7(a) and 7(b), the real and imaginary parts of the wave function, A and B, are plotted in Fig. 7(c). Because both A and B are smooth near $x=1.12$ a.u., there is no difficulty is computing their derivatives.

Use of the (A,B) representation does not lead to the hydrodynamic equations that were described earlier in Sec. II,

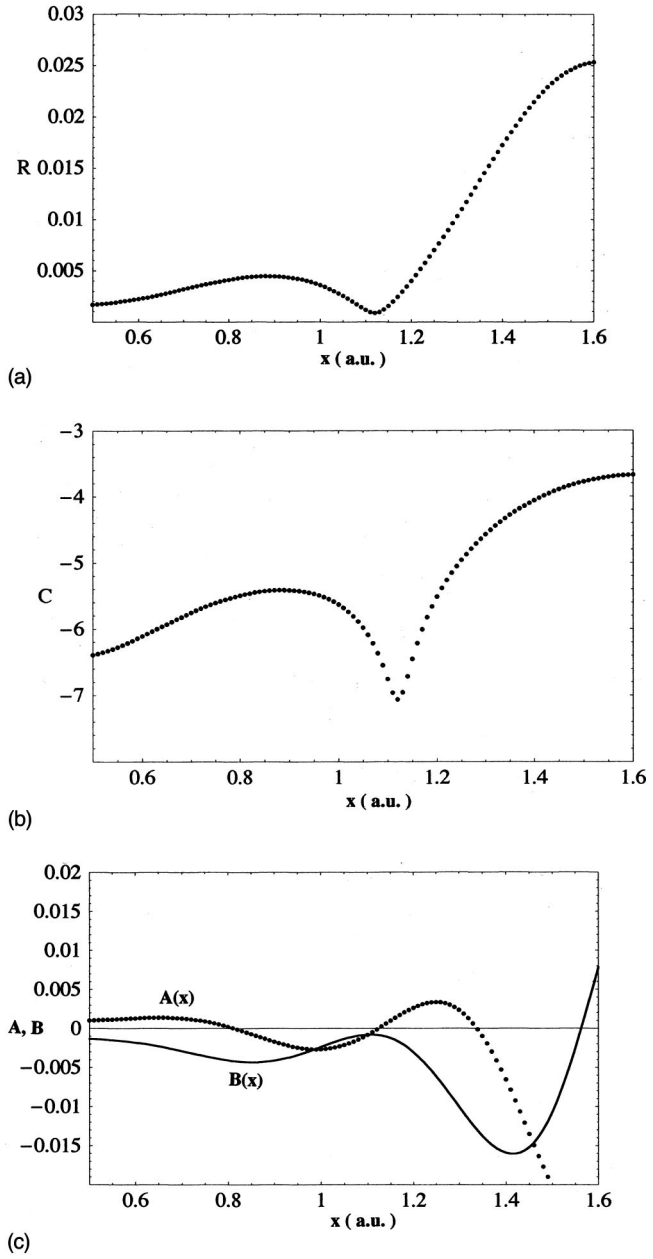

FIG. 7. Scattering wave function at time step 510 ($t=49.4$ fs). (a) The R-amplitude; (b) the C-amplitude; (c) the real and imaginary parts of the wave function, A and B, respectively. The quasinode near $x=1.12$ a.u. should be noted.

but in regions around nodes this representation has the advantage that there is no difficulty in computing derivatives. The hybrid scheme that will be followed in this study is based upon use of the (C,S) hydrodynamic representation in all regions, except for patches near nodes or quasinodes. In these nodal regions, the (A,B) representation will be used.

The way in which these two representations are used is illustrated in Fig. 5. We will assume that a quasinode has developed near $x=1.3$ near the center of the figure. In the grid adaptation step, 11 equally spaced points were inserted between the boundary particles labeled M_0 and M_1. The (A,B) region extends from points M_0+1 to M_1-1 and wave function values at the boundary points M_0 and M_1 are used to feed information from the outer (C,S) regions to the inte-

rior region. In addition, the (R,S) region extends from the left of the figure to point M_0+3 and then continues from point M_1-3 to the right of the figure. In the two overlap patches encompassing points M_0+1 through M_0+3 on the left and points M_1-3 through M_1-1 on the right, the wave functions separately computed in the two exterior (C,S) regions and in the middle (A,B) region can be smoothly blended by averaging the wave functions. The size of the blending patches is rather arbitrary and will need to be determined through experience.

B. Propagation in the (*A,B*) representation

We have mentioned that the real and imaginary parts of the wave function, denoted (A,B), will be used in the interior of the local region Γ between the boundary particles labeled M_0 and M_1. For the boundary particles and all particles exterior to Γ the quantum hydrodynamic equations will be integrated to find the particle trajectories. However, within region Γ, a propagation technique will be used to advance the values of (A,B) to the next time step. The time-evolution problem in the internal region is both an initial value problem and a 2-point Dirichlet boundary value problem. The initial values are those which have been interpolated onto the adapted mesh at time t, and the boundary values are those supplied at the points M_0 and M_1 from the hydrodynamic propagation. The propagation algorithm used in this study for the internal region is the unconditionally stable (and implicit) Crank–Nicholson (CN) scheme.[30] This scheme can handle the two-point boundary problem and propagates (A,B) from one time step to the next.

In operator form, the CN algorithm starts with $\psi(x,t)$ and generates $\psi(x,t+\Delta t)$ according to

$$\left(1+\frac{\Delta t}{2\hbar}\hat{H}\right)\psi(t+\Delta t)=\left(1-\frac{\Delta t}{2\hbar}\hat{H}\right)\psi(t), \tag{13}$$

where $\hat{H}$ is the Hamiltonian operator. After substituting the decomposition of the wave function into real and imaginary parts, we obtain coupled real-valued equations for A and B,

$$B(x,t+\Delta t)+\frac{\Delta t}{2\hbar}\hat{H}A(x,t+\Delta t)=B(x,t)-\frac{\Delta t}{2\hbar}\hat{H}A(x,t),$$

$$A(x,t+\Delta t)-\frac{\Delta t}{2\hbar}\hat{H}B(x,t+\Delta t)=A(x,t)+\frac{\Delta t}{2\hbar}\hat{H}B(x,t).$$

At this point, we introduce the finite-difference discretization of the x-coordinate, with the uniform grid spacing Δx. Using a central second-difference approximation for ∇^2, these two equations become a system of $2N$ (where N is the number of grid points in the internal region) linear algebraic equations. When setting up these equations, the values of A and B at two times, t and $t+\Delta t$, at the two end points, M_0 and M_1, are required. These eight required boundary values are obtained form the hydrodynamic equations-of-motion. This procedure is repeated for each time step that the local adaptive grid is used.

VI. COMPUTATIONAL RESULTS

In this section, results will be presented to illustrate grid adaptation for the portion of the wave packet undergoing reflection from the Eckart barrier. First, several details will be mentioned concerning implementation of the grid adaptation scheme described earlier in Sec. IV. With reference to Fig. 5, for the results reported here, the (C,S) region was chosen not to overlap the (A,B) region; all points interior to those labeled M_0 and M_1 were included in the (A,B) representation. Finally, in order to interpolate data from the unstructured mesh onto the uniform mesh in the adapted region, a method based upon Lagrange interpolation polynomials was used. This method is described in the book by Fornberg,[31] and a corrected version[32] of SUBROUTINE WEIGHTS1 from Appendix C was employed with the parameter value $n=7$.

Because of inflation (associated with node formation) and compression that occurs in advance of the central portion of the wave packet as well as ''thinning out'' that occurs in the wake behind the peak (this is not due to node formation), a rather large region was selected for adaptation. Figure 8(a) shows the real part of the scattering wave function at time step 470 (the same time step that was used for Fig. 1), with inflation and compression clearly displayed between $x=1.0$ a.u. and $x=4.0$ a.u. Thinning in the wake between $x=4.5$ a.u. and $x=7$ a.u. is also evident. The region selected for adaptation lies between points $M_0=6$ and $M_1=80$ and these are shown by the large black dots in Fig. 8(a). (Particle 81, on the far right of the figure, will just trail along behind the adapted region as it moves to the left.) With both $A(x)$ and $B(x)$ given as input on the unstructured grid between M_0 and M_1, these two functions were then interpolated onto a uniform mesh lying between these two boundary points. The adapted mesh and the original mesh were chosen to have the same number of points between the boundary points, so that redistribution is the technique being used in this illustration of grid adaptation.

Using the Crank–Nicholson algorithm to update the values for (A,B) in the internal region and integrating the hydrodynamic equations-of-motion to find the particle positions in the exterior region, the time evolution of the system is obtained. Figures 8(b) and 8(c) show the real part of the scattering wave function after propagating an additional 25 or 75 time steps, respectively. Over the time interval between Figs. 8(a) and 8(c), the central peak in $A(x)$ propagates about 0.8 a.u. toward the left of the figure. Before introduction of the adapted grid, it was only possible to advance about 10 time steps beyond that shown in Fig. 8(a). At that time, numerical problems developing around the nodes led to particle crossings (interchange of position in one dimension) and subsequently the code crashed. Introduction of the adapted grid in the region of extensive inflation and compression thus permitted propagation to longer times then could be obtained when only the hydrodynamic representation was employed. By adjusting the various parameters, propagation to times later than shown in Fig. 8(c) could be obtained, but the plots are very similar to those shown here. The parameters that were varied included the following: (1) the size of the region over which adaptation was employed; (2) the starting time-

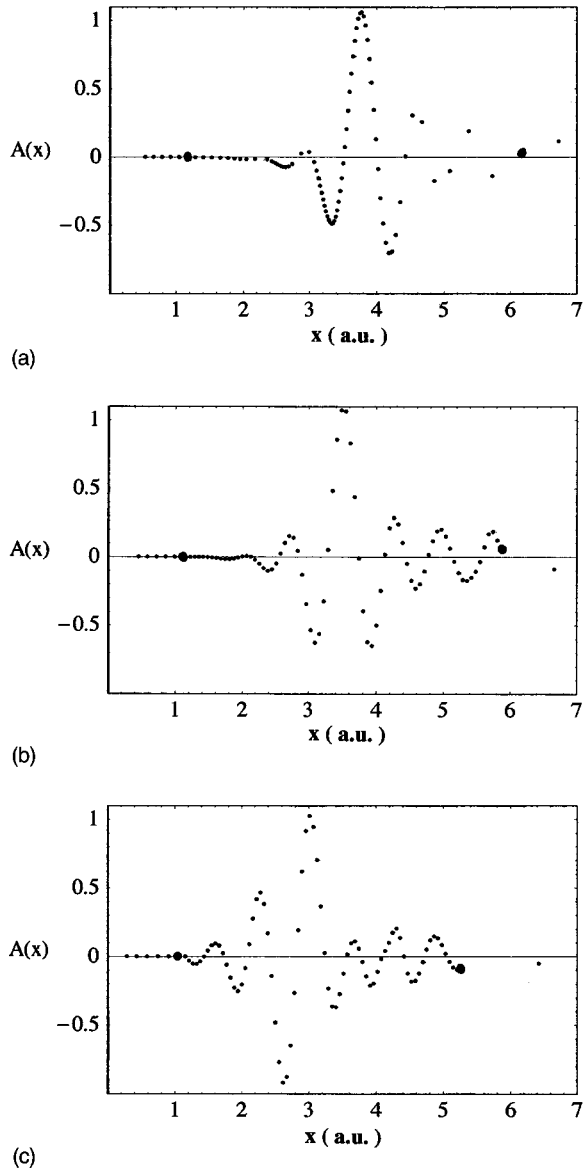

FIG. 8. Real part of the scattering wave function at time steps (a) 470, (b) 495, and (c) 545. The left and right boundary particles for the adaptation region are shown as large dots. In (a), the unstructured particle locations are shown by the dots, while in (b) and (c) the adapted mesh is used between the boundary points.

step for initiating the adaptation process; (3) the number of adapted mesh points used in the internal region. The important point is that the ''node problem'' occurring in the hydrodynamic formulation has been circumvented. Further experimentation on this and other scattering and bound state problems would be very worthwhile.

VII. SUMMARY

Discretization of the hydrodynamic equation-of-motion leads to an appealing picture of quantum mechanical time evolution: particles follow quantum trajectories. These particles (actually, elements of the probability fluid) move under the influence of classical ($f_c = -\nabla V$) and quantum ($f_q = -\nabla Q$) forces. Because of the nonlocal quantum force, the particles move together as a correlated ensemble, even when the classical force vanishes. As the distribution of particles evolves in time, highly nonuniform distributions are frequently generated. These nonuniform distributions show both compression and inflation; these are regions where particles tend to aggregate or avoid. Regions around wave function nodes always show inflation, but other regions (such as the tails of wave packets) may also show low particle densities. Because of the low density and nonuniform particle distribution around these nodes, accurate calculation of the quantum potential and the quantum force presents severe challenges to algorithms designed for calculating derivatives.

In order to meet the challenges posed by highly nonuniform particle distributions, adaptive Lagrangian (moving) grids were introduced in this study. Using diagnostic tools, patches can be identified where trouble may later develop during the time evolution. Within these local patches, grid adaptation can add, remove, or redistribute mesh points as necessary. In addition, in patches which surround wave function nodes, the hydrodynamic representation is abandoned in favor of propagation in terms of the real and imaginary parts of the wave function, denoted A and B, respectively. Problems encountered in the hydrodynamic representation with calculating the derivatives of the wave function amplitude, $R=(A^2+B^2)^{1/2}$, are circumvented. The use of the (A,B) wave function representation in local patches along with the hydrodynamic representation in all other regions leads to a mixed representation which still permits propagation of particles. Within the local patches, the local velocity field can be computed from A and B, and the particles trajectories can be extended through these regions.

In this study, grid adaptation was applied to the reflected portion of a wave packet scattering from a repulsive Eckart potential. During reflection, a series of transient nodes form in the leading edge of this wave packet. When using the hydrodynamic representation, it was not possible to propagate beyond the early stage of formation of the first node in the reflected wave packet. However, using the (A,B) representation of the wave function within the region where grid adaptation was introduced permitted propagation to much later times. Further investigation is needed to tune the diagnostic tools that can be used to determine when and where to perform grid adaptation. In addition, further studies are needed to determine whether to redistribute grid points, or whether to add or remove points to achieve a better sampling of the data used in computing derivatives required for solving the equations-of-motion.

ACKNOWLEDGMENTS

We wish to thank Professors Donald Kouri (University of Houston), David Hoffman (Iowa State University), Bala Ramachandran (Louisiana Tech University), and Dr. Pablo Yepes (Rice University) for helpful conversations. In addition, Courtney Lopreore, Kyungsun Na, and Fernando Sales Mayor are thanked for their comments. R.E.W. and E.R.B. both thank the National Science Foundation and the Robert Welch foundation for research support. R.E.W. also thanks the Texas Advanced Computing Center at the University of Texas for access to the Cray SV 1. E.R.B. also thanks the Texas Higher Education Coordinating Board's Advanced Research Program and the NSF for a CAREER award.

[1] E. Madelung, Z. Phys. **40**, 322 (1926).
[2] L. de Broglie, C. R. Séances Acad. Sci. **183**, 447 (1926); **184**, 273 (1927).
[3] D. Bohm, Phys. Rev. **85**, 166 (1952); **85**, 180 (1952).
[4] D. Bohm, B. J. Hiley, and P. N. Kaloyerou, Phys. Rep. **144**, 321 (1987).
[5] D. Bohm and B. J. Hiley, *The Undivided Universe* (Routeledge, London, 1993).
[6] D. Bohm, B. J. Hiley, and P. N. Kaloyerou, Phys. Rep. **144**, 321 (1987).
[7] P. R. Holland, *The Quantum Theory of Motion* (Cambridge University Press, New York, 1993).
[8] H. E. Wilhelm, Phys. Rev. D **1**, 2278 (1970).
[9] C. Philippidis, C. Dewdney, and B. J. Hiley, Nuovo Cimento Soc. Ital. Fis., B **52B**, 15 (1979).
[10] J. H. Weiner and Y. Partom, Phys. Rev. **187**, 1134 (1969).
[11] J. H. Weiner and A. Askar, J. Chem. Phys. **54**, 1108 (1971); **54**, 3534 (1971).
[12] C. Lopreore and R. E. Wyatt, Phys. Rev. Lett. **82**, 5190 (1999).
[13] F. Sales Mayor, A. Askar, and H. A. Rabitz, J. Chem. Phys. **111**, 2423 (1999).
[14] C. Lopreore and R. E. Wyatt, Chem Phys. Lett. **325**, 73 (2000).
[15] R. E. Wyatt, J. Chem. Phys. **111**, 4406 (1999).
[16] R. E. Wyatt, Chem. Phys. Lett. **313**, 189 (1999).
[17] D. K. Hoffman and D. J. Kouri, in *Proceedings of the 3rd International Conference on Mathematical and Numerical Aspects of Wave Propagation* (SIAM, Philadalphia, 1995).
[18] D. K. Hoffman, T. L. Marchioro II, M. Arnold, Y. Huang, W. Zhu, and D. J. Kouri, J. Math. Chem. **20**, 117 (1996).
[19] R. E. Wyatt, D. Kouri, and D. Hoffman, J. Chem. Phys. **112**, 10730 (2000).
[20] E. R. Bittner, J. Chem. Phys. **112**, 9703 (2000).
[21] E. R. Bittner and R. E. Wyatt, J. Chem. Phys. **113**, 8888 (2000), previous paper.
[22] M. J. Fritts, W. P. Crowley, and H. Trease, *The Free-Lagrange Method* (Springer-Verlag, New York, 1985).
[23] H. Trease, M. J. Fritts, and W. P. Crowley, *Advances in the Free-Lagrange Method* (Springer-Verlag, New York, 1990).
[24] P. A. Zegeling, in *Handbook of Grid Generation*, edited by J. F. Thompson, B. K. Soni, and N. P. Weatherill (CRC, New York, 1999).
[25] G. F. Carey, *Computational Grids* (Taylor and Francis, Washington, D.C., 1997).
[26] Y. Kallinderis, *Grid Adaptation by Redistribution and Local Embedding*, Lecture notes for the 27th Computational Fluid Dynamics Lecture Series (Von Karmen Institute, Brussles, 1996).
[27] X. Gallez, P. Halin, G. Lielens, R. Keunings, and V. Legat, Comput. Methods Appl. Mech. Eng. **180**, 345 (1999).
[28] P. MacNeice, K. M. Olson, C. Mobarry, R. de Fainchtein, and C. Packer, Comput. Phys. Commun. **126**, 330 (2000).
[29] N. Pinto-Neto and E. Santini, Phys. Rev. D **59**, 123517 (1999).
[30] C. A. J. Fletcher, *Computational Techniques for Fluid Dynamics* (Springer-Verlag, New York, 1991).
[31] B. Fornberg, *A Practical Guide to Pseudospectral Methods* (Cambridge University Press, New York, 1996).
[32] The corrected subroutine may be obtained by contacting the authors of this study.